Soft-Tissue Simulation for Cranio-Maxillofacial Surgery: Clinical Needs and Technical Aspects

Hyungmin Kim, Philipp Jürgens and Mauricio Reyes

Abstract Computerized soft-tissue simulation can provide unprecedented means for predicting facial outlook pre-operatively. Surgeons can virtually perform several surgical plans to have the best surgical results for their patients while considering corresponding soft-tissue outcome. It could be used as an interactive communication tool with their patients as well. There has been comprehensive amount of works for simulating soft-tissue for cranio-maxillofacial surgery. Although some of them have been realized as commercial products, none of them has been fully integrated into clinical practice due to the lack of accuracy and excessive amount of processing time. In this chapter, state-of-the-art and general workflow in facial soft-tissue simulation will be presented, along with an example of patient-specific facial soft-tissue simulation method.

1 Introduction

1.1 Facial Aesthetics

The human face is the most complex anatomical, physiological and functional region of the body. The senses of vision, hearing, smell and taste are concentrated in the facial region. And the skin of the face has the highest number of sensibility receptors. The oral cavity serves for ingestion and creation of speech and the upper airway allows respiration. Twenty-eight mimic muscles help to express emotions and thoughts. The face is the most important part of the body that helps us to

H. Kim · P. Jürgens · M. Reyes (✉)
University of Bern, Bern, Switzerland
e-mail: mauricio.reyes@istb.unibe.ch

Stud Mechanobiol Tissue Eng Biomater (2012) 9: 413–440
DOI: 10.1007/8415_2011_105

Published Online: 9 October 2011

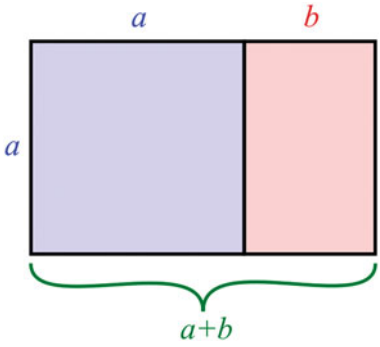

Fig. 1 Golden rectangle (Source: Wikipedia)

identify other people and recognize in unknown person's gender, approximate age and even constitution. While a disfigured face impresses and causes certain reactions on a beautiful face fascinates and attracts them.

In general beauty is associated with other positive characteristics: we think that a beautiful person is more likable, communicative, successful and popular than others. But how can we define beauty? David Hume's statement "Beauty exists merely in the mind which contemplates them" [18] is a contradiction to the attempt of defining objective standards for beauty. But if an intercultural comparison is applied, there is a high accordance about the perception of an aesthetic facial appearance among ethnical groups and different age classes [9, 30]. Even little children are more attracted to attractive adults, than to not-attractive individuals [29].

Over the past centuries various disciplines in science and arts have tried to answer the question which criteria make a face attractive. The face of a human being is considered to be attractive if it presents the following properties:

- Symmetry [18]
- Average [29]
- Individual characteristics [8]

An average face means a facial appearance close to the mean of the population. If an unknown person presents an average face the person seems familiar to the opponent, because it corresponds to the previously learned mean of the category facial appearance [28]. The average face is subconsciously associated with a good phenotype meaning that the stabilizing effect of natural selection of certain facial appearances is recognized [53].

Comparable factors can be detected when analyzing symmetry: symmetric facial proportions indicate healthy genes. It is even supposed that this is a characteristic for a higher resistance against parasites [53].

In contrary to symmetry and average, certain unique characteristics allow us to recognize an individual face, which is essential for the perception of an individual and the development of a personal identity [8].

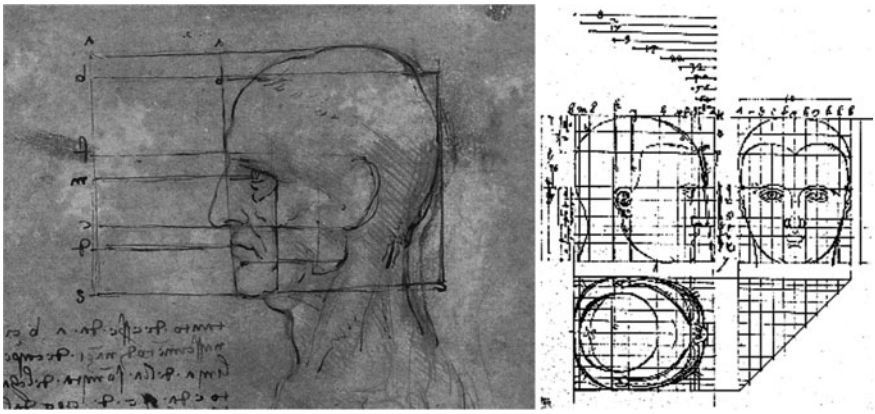

Fig. 2 Proportions of the human head: Leonardo da Vinci (*left*) (Source: Wikipedia), Albrecht Dürer (*right*) [12]

Besides symmetry and average an extremely important factor are proportions. The embodiment of harmonic and aesthetic proportions and even mathematical beauty is the golden ratio mainly applied in architecture and arts.

$$\frac{a+b}{a} = \frac{a}{b} \equiv \varphi = \frac{1+\sqrt{5}}{2} = 1.6180339887\ldots \tag{1}$$

When analyzing facial proportions, we also find proportions close to the golden ratio (Fig. 1): most famous are the proportion analysis of Albrecht Dürer and Leonardo da Vinci as in Fig. 2.

1.2 Cranio-Maxillofacial Surgery

Cranio-maxillofacial (CMF) surgery is a surgical specialty that deals with the treatment of inborn or acquired facial disfigurements. These conditions can be such as cleft lip- and palate, craniofacial malformations, aftermath of facial trauma or of ablative tumor surgery. Surgical interventions in the CMF area and even their planning make high demands on the spatial sense of the surgeons. This is on one the hand due to the close proximity of highly vulnerable anatomical structures and on the other hand due to the complex morphology of the region. Modern image-guided techniques are the basis for diagnostics, therapy and documentation. These technologies enable us to produce patient-specific models of the clinical situation. They give us the possibility to perform accurate planning and transfer the planning to the operation theatre. These technologies have made their way into the clinical routine of highly advanced treatment centers [6, 13, 20, 21, 22, 40]. One of the most evident indications for the use of virtual planning tools in CMF Surgery is the planning of surgical intervention

for patients suffering of malocclusion. Malocclusion can either be caused by a malposition of teeth in the level of the alveolar crest or by an incorrect positioning of the upper and lower jaw relative to each other. For the former, an orthodontic treatment will deliver satisfactory results. For the latter, only a surgical procedure will provide a causal therapy. These interventions are called orthognathic surgeries and their aim is to change the position of the maxillary and mandibular bone, relative to each other and to the skull base [1, 10, 17]. As these interventions are highly elective, an accurate and extensive preoperative planning has to be conducted. The technique for planning and performing the simultaneous relocation of maxilla and mandible was first described in 1970 by Obwegeser [43]. To update the planning procedure several systems for virtual three-dimensional visualization and procedure planning based on volume datasets have been recently introduced in some clinical centers, routinely substituting the conventional two-dimensional cephalogram based planning-approach, and especially improving the prediction of soft tissue deformations [3, 42, 54, 57, 58]. In order to ensure an optimal pre-operative skeletal planning of the patient with his postoperative facial appearance, a highly reliable and accurate prediction system is required [25, 26].

In order to realize the pre-operative surgical plan in the operation theatre, the planning and prediction software should be linked to navigation system for the intra-operative control of the relocation of the upper and lower jaw [6, 20, 22, 61]. As a consequence, a planning console for CMF surgery should contain the following modules to cover all the clinical requirements:

- Import module of DICOM data
- User-friendly segmentation and mesh modeling
- Module for virtual osteotomy and relocation of bone segments
- Three-dimensional cephalometry
- Fast and accurate soft-tissue simulation
- Connection to intra-operative navigation system

1.3 Soft-Tissue Simulation in CMF Surgery: State-of-the-Art

There have been already extensive amount of studies in order to overcome the difficulty in soft-tissue modeling. Vannier et al. [56] originally introduced the idea of predicting post-operative facial appearance for CMF surgery using computer-assisted approach. Later, face modeling was intensively studied by the computer graphics community, whose main interest was in simulating facial expressions in real-time. Terzopoulos et al. [50] and Lee et al. [32] suggested multi-layered facial tissue model consisting of mass-spring elements. On the other hand, Koch et al. [27] suggested a non-linear finite-element approach using C^1-continuous surface element and linear springs connected to bony structures. Keeve et al. [24]

presented a Mass-Spring Model (MSM) with prismatic element, and compared the result with Finite-Element Model (FEM) in terms of accuracy and computational cost. Sarti et al. [48] proposed a voxel-based FEM approach based on a super computer, which can be directly applied to voxel grid of the Computed Tomography (CT) data at the cost of large memory space. Zachow et al. [59] suggested a fast tetrahedral volumetric FEM, which can be applicable to clinical practice. Later, Gladilin et al. [16] extended this to functional simulation with facial muscles. Alternatively, Cotin et al. [7] proposed a hybrid method using Mass-Tensor Model (MTM) for enhanced local deformations in simulation of surgical sites. Later, MTM was extended to non-linear, anisotropic elasticity by Picinbono et al. [46]. Chabanas et al. [5] proposed a mesh morphing algorithm to minimize the laborious efforts on preparing finite-element mesh. Mollemans et al. [39] first applied MTM to CMF soft-tissue simulation, and the method was qualitatively and quantitatively evaluated on ten clinical cases. Some of the previously developed methods have been realized as commercial products, e.g. SurgiCase CMF (Materialise, Leuven, Belgium), Maxilim (Medicim NV, Mechelen, Belgium), Dolphin 3D Surgery (Dolphin Imaging & Management Systems, Chatsworth, CA), 3dMDvultus (3dMD, Atlanta, Ga), In Vivo (Anatomage Inc, San Jose, CA).

Even though considerable amount of research has been conducted for resolving soft-tissue simulation, up to our knowledge none of it has been fully integrated into the clinical workflow, due to insufficient accuracy or excessive processing time required for simulation. The state-of-the-art simulation results around error-sensitive regions, such as nose and lips area, are still far from clinical reality, e.g. nose tip stays in stationary position under the effect of considerable movements of the underlying skeletal segments. This results in the need for patient-specific simulation strategy, that considers individual facial muscular structures for soft-tissue simulation. At the same time, the excessive amount of processing time for patient-specific modeling should be avoided, in order to render the developed method useful for daily clinical practice. Accordingly, a simulation framework enabling reduced modeling efforts, and enhanced computational performance is anticipated. Fortunately, rapid development in computing hardware, e.g. multi-core central processing unit (CPU) or graphics processing unit (GPU), makes this situation favorable.

1.4 Computational Models for Soft-Tissue Simulation

The computational methods, developed for simulating soft-tissues behavior so far, can be categorized into the following three types: MSM, FEM, and MTM. MSM is known to be the most computationally efficient method due to its simplicity in physics. However, the coarse approximation of true physics is not suitable for surgical planning. On the other hand, the mathematical background of FEM is based on continuum mechanics, and its utmost accuracy has been proved in other

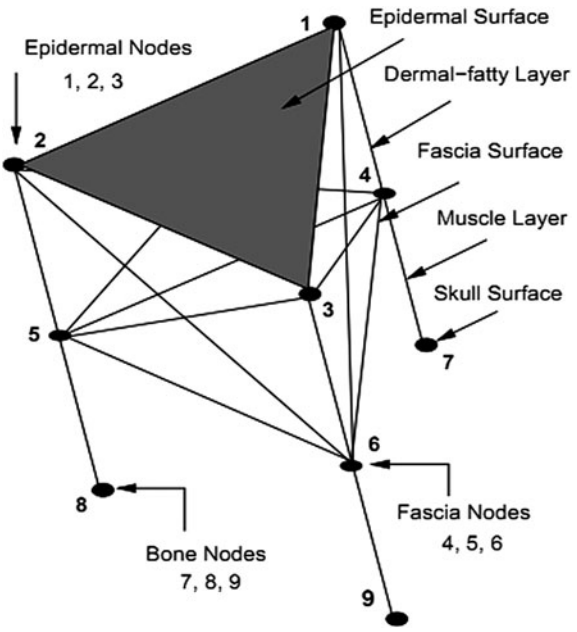

Fig. 3 Multi-layered mass-spring model (Source: Lee et al. [32])

scientific applications. However, it usually requires considerable amount of time for preparation of mesh and computation of soft-tissue deformations. This makes FEM hard to be used in daily clinical applications without using specialized hardware-specific implementation. MTM was developed as a golden mean between MSM and FEM, which is known to be bio-mechanically relevant as FEM, and computationally efficient as MSM. Those models have been actively used in various applications with its unique features, although recent developments in computation hardware has bridged the gap between these strategies.

1.4.1 Mass-Spring Model

In MSM, the object is discretized into mass points and inter-connections between each of these mass points. As shown in Fig. 3, layer-based MSM has been widely used for characterizing multiple soft-tissue layers, e.g. epidermis, dermis, SMAS (Superficial Muscular Aponeurotic System), fascia and muscles.

The governing equation for MSM can be described by Eq. 2 and is known as Hooke's law, where the elastic forces $\mathbf{f}_s$ is proportional to the changes in length of the spring element ΔL between the actual and the rest status at the rate of spring constant k_s.

$$\mathbf{f}_s = k_s \Delta L \tag{2}$$

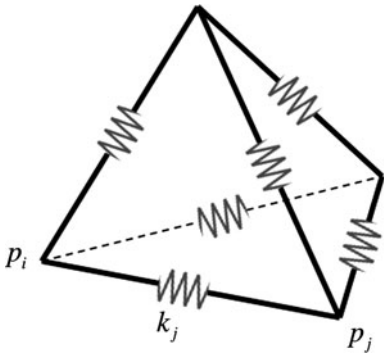

Fig. 4 Tetrahedral mass-spring model: 3D coordinate of point i and j ($\mathbf{p}_i, \mathbf{p}_j$), spring constant of connecting spring k_j

Alternatively, tetrahedral-based MSM was proposed by Mollemans et al. [37], where automatic mesh generation method can be used for constructing volumetric meshes from surface meshes. The governing equation can be expressed by Eq. 3, which correlates the total internal elastic force of point i ($\mathbf{f}_i^{int}$) with the set of vertices connected to the mass point i (Ψ_i), 3D coordinate of point i and j ($\mathbf{p}_i, \mathbf{p}_j$), the length of the spring at rest L_j^0, and spring constant of connecting spring k_j as shown in Fig. 4.

$$\mathbf{f}_i^{int} = \sum_{\forall \mathbf{p}_j \in \Psi_i} k_j \left(\| \mathbf{p}_j - \mathbf{p}_i \| - L_j^0 \right) \frac{\mathbf{p}_j - \mathbf{p}_i}{\| \mathbf{p}_j - \mathbf{p}_i \|} \tag{3}$$

According to Van Gelder et al. [15], the spring constant of spring can be expressed by

$$k_j = \frac{E \sum_{e \in \Lambda_j} V_e}{(L_j^0)^2} \tag{4}$$

where Λ_j is the collection of all neighboring tetrahedra containing spring j, V_e is the initial volume of the neighboring tetrahedra, and L_j^0 is the initial length of the spring.

Since there is little interest in the transient phase of the deformation for CMF soft-tissue simulation, the direct computation approach proposed by Teschner et al. [52] can be used, which enables the deformation to be computed in iterative ways by setting the internal force in equilibrium state to be zero.

1.4.2 Finite-Element Model

Soft-tissue simulation can be regarded as the task of finding the displacement vector field which maps all points in initial shape to deformed shape, where the deformation caused by the displacements or forces on the boundary, described by the deformation function $\Phi(\mathbf{x})$ as shown in Fig. 5.

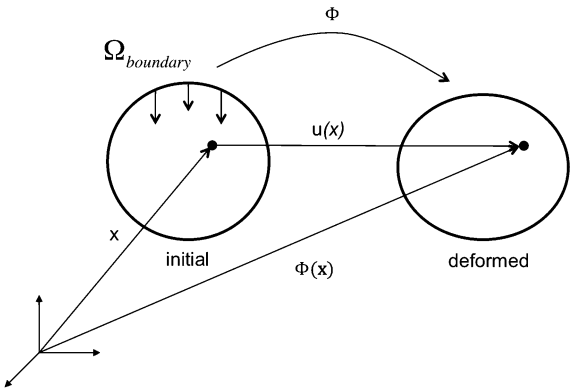

Fig. 5 Problem description of soft-tissue simulation: the deformation function $\Phi(\mathbf{x})$, displacement vector $\mathbf{u}$, spatial position vector $\mathbf{x}$, domain for boundary condition $\Omega_{boundary}$

The displacement vector $\mathbf{u}$ is defined by

$$\mathbf{u} = \Phi(\mathbf{x}) - \mathbf{x} \tag{5}$$

The change of metric in the deformed body can be measured by the right Cauchy-Green deformation tensor $\mathbf{C}$, which are expressed by the deformation gradient.

$$\mathbf{C} = \nabla\Phi^T \nabla\Phi \tag{6}$$

The amount of deformation can be expressed by the 3×3 Green-Lagrange strain tensor $\mathbf{E}(\mathbf{x})$, whose diagonal terms represent the length variation and off-diagonal terms state the shear effect along the three axes.

$$\mathbf{E} = \frac{1}{2}(\mathbf{C} - \mathbf{I}) = \frac{1}{2}\left(\nabla\Phi^T \nabla\Phi - I\right) \tag{7}$$

According to Eq. 5, $\nabla\Phi = I + \nabla\mathbf{u}$ can be deduced, and Eq. 7 can be expressed as

$$\mathbf{E} = \frac{1}{2}\left((I + \nabla\mathbf{u})^T (I + \nabla\mathbf{u}) - I\right) = \frac{1}{2}\left(\nabla\mathbf{u} + \nabla\mathbf{u}^T + \nabla\mathbf{u}^T \nabla\mathbf{u}\right) \tag{8}$$

Assuming small displacements, linearized Green-Lagrange strain tensor $\mathbf{E}_L$ can be used:

$$\mathbf{E}_L = \frac{1}{2}\left(\nabla\mathbf{u} + \nabla\mathbf{u}^T\right) = \begin{bmatrix} \varepsilon_{xx} & \frac{\gamma_{xy}}{2} & \frac{\gamma_{xz}}{2} \\ \frac{\gamma_{xy}}{2} & \varepsilon_{yy} & \frac{\gamma_{yz}}{2} \\ \frac{\gamma_{xz}}{2} & \frac{\gamma_{yz}}{2} & \varepsilon_{zz} \end{bmatrix} \tag{9}$$

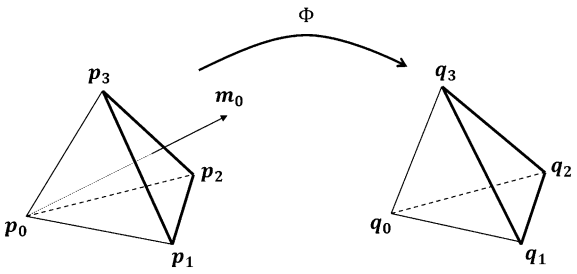

Fig. 6 Deformation of tetrahedral element

The constitutive equation for a linear isotropic material is given by Hooke's law [13]:

$$\begin{bmatrix} \sigma_{xx} \\ \sigma_{yy} \\ \sigma_{zz} \\ \sigma_{xy} \\ \sigma_{yz} \\ \sigma_{zx} \end{bmatrix} = \begin{bmatrix} \lambda+2\mu & \lambda & \lambda & 0 & 0 & 0 \\ \lambda & \lambda+2\mu & \lambda & 0 & 0 & 0 \\ \lambda & \lambda & \lambda+2\mu & 0 & 0 & 0 \\ 0 & 0 & 0 & \mu & 0 & 0 \\ 0 & 0 & 0 & 0 & \mu & 0 \\ 0 & 0 & 0 & 0 & 0 & \mu \end{bmatrix} \begin{bmatrix} \varepsilon_{xx} \\ \varepsilon_{yy} \\ \varepsilon_{zz} \\ \gamma_{xy} \\ \gamma_{yz} \\ \gamma_{zx} \end{bmatrix} \Leftrightarrow \sigma = \mathbf{D}\varepsilon \tag{10}$$

where Lamé coefficients λ and μ are expressed in relationship with Young's modulus E and Poisson's ratio v :

$$\lambda = \frac{Ev}{(1+v)(1-2v)} \tag{11}$$

$$\mu = \frac{E}{2(1+v)} \tag{12}$$

FEM theory explains that the elastic deformation of the entire object can be described by the elastic behavior of each element descritizing the object. Therefore, the displacement **u** inside the linear tetrahedral element shown in Fig. 6 can be expressed as a linear combination of the displacements of the four vertices of the tetrahedron:

$$\mathbf{u} = \sum_{k=0}^{3} \mathbf{N}_k^e \mathbf{u}_k^e = \mathbf{N}^e \mathbf{u}^e \tag{13}$$

where

$$N_k^e = \frac{a_k + b_k x + c_k y + d_k z}{6V^e},$$

here V^e is the volume of the tetrahedron, and a_k, b_k, c_k, d_k are defined by

$$
\begin{aligned}
a_k &= \begin{vmatrix} x_{k+1} & y_{k+1} & z_{k+1} \\ x_{k+2} & y_{k+2} & z_{k+2} \\ x_{k+3} & y_{k+3} & z_{k+3} \end{vmatrix} \\
b_k &= \begin{vmatrix} 1 & y_{k+1} & z_{k+1} \\ 1 & y_{k+2} & z_{k+2} \\ 1 & y_{k+3} & z_{k+3} \end{vmatrix} \\
c_k &= -\begin{vmatrix} x_{k+1} & 1 & z_{k+1} \\ x_{k+2} & 1 & z_{k+2} \\ x_{k+3} & 1 & z_{k+3} \end{vmatrix} \\
d_k &= -\begin{vmatrix} x_{k+1} & y_{k+1} & 1 \\ x_{k+2} & y_{k+2} & 1 \\ x_{k+3} & y_{k+3} & 1 \end{vmatrix}
\end{aligned} \tag{14}
$$

The strain ε in Eq. 10 can be expressed as:

$$
\varepsilon = \begin{bmatrix} \varepsilon_{xx} \\ \varepsilon_{yy} \\ \varepsilon_{zz} \\ \gamma_{xy} \\ \gamma_{yz} \\ \gamma_{zx} \end{bmatrix} = \begin{bmatrix} \frac{\partial u}{\partial x} \\ \frac{\partial v}{\partial y} \\ \frac{\partial w}{\partial z} \\ \frac{\partial u}{\partial y} + \frac{\partial v}{\partial x} \\ \frac{\partial v}{\partial z} + \frac{\partial w}{\partial y} \\ \frac{\partial u}{\partial z} + \frac{\partial w}{\partial x} \end{bmatrix} = \mathbf{B}\mathbf{u}^e = [\mathbf{B}_k \mathbf{B}_{k+1} \mathbf{B}_{k+2} \mathbf{B}_{k+3}]\mathbf{u}^e \tag{15}
$$

where $\mathbf{B}_k$ is expressed by

$$
\mathbf{B}_k = \begin{bmatrix} \frac{\partial N_k}{\partial x} & 0 & 0 \\ 0 & \frac{\partial N_k}{\partial y} & 0 \\ 0 & 0 & \frac{\partial N_k}{\partial z} \\ \frac{\partial N_k}{\partial y} & \frac{\partial N_k}{\partial x} & 0 \\ \frac{\partial N_k}{\partial z} & 0 & \frac{\partial N_k}{\partial x} \end{bmatrix} = \frac{1}{6V^e} \begin{bmatrix} b_k & 0 & 0 \\ 0 & c_k & 0 \\ 0 & 0 & d_k \\ c_k & b_k & 0 \\ 0 & d_k & c_k \\ d_k & 0 & b_k \end{bmatrix} \tag{16}
$$

The principle of virtual work gives the relationship between the work done by the internal stresses and external work performed by the elastic force in equilibrium state:

$$
\delta \mathbf{u}^{e^T} \mathbf{q}^e = \int_{V^e} \delta \varepsilon^T \sigma dV \tag{17}
$$

where $\mathbf{q}^e$ is the elastic force vector, $\delta \mathbf{u}^e$ is the virtual displacement vector.

Combined with Eq. 16, the following equation is deduced.

$$
\delta \mathbf{u}^{e^T} \mathbf{q}^e = \int_{V^e} (\mathbf{B}\delta \mathbf{u}^e)^T \sigma dV = \delta \mathbf{u}^{e^T} \int_{V^e} \mathbf{B}^T \sigma dV \tag{18}
$$

Since Eq. 18 must be valid for any virtual displacement $\delta \mathbf{u}^e$,

$$\mathbf{q}^e = \int_{V^e} \mathbf{B}^T \sigma dV = \mathbf{K}^e \mathbf{u}^e \tag{19}$$

where $\mathbf{K}^e = \int_{V^e} \mathbf{B}^T \mathbf{D} \mathbf{B} dV$

The total elastic force $\mathbf{F}_k$ on vertex k can be obtained by summing the elastic force contributions of neighboring tetrahedra containing vertex k:

$$\mathbf{F}_k = \sum_{\forall j \in \Omega_k} \mathbf{q}_k^j = \sum_{\forall j \in \Omega_k} \mathbf{K}^j \mathbf{u}^j \tag{20}$$

Combining Eq. 20 in matrix form for m vertices:

$$\mathbf{F} = \mathbf{K}\mathbf{u} \tag{21}$$

where elastic force vector $\mathbf{F}$ and displacement vector $\mathbf{u}$ have dimension of $(m \times 3) \times 1$, and $\mathbf{K}$ is called the global stiffness matrix.

For all joined vertices which we know the displacements, the boundary condition is given as,

$$\mathbf{u}_k = \mathbf{u}_k^0 \tag{22}$$

For all free vertices where displacements need to be updated,

$$\mathbf{F}_k = 0 \tag{23}$$

Since the global matrix $\mathbf{K}$ is very sparse whose element $\mathbf{K}_{ij}$ is only non-zero if model point i and j are vertices of a common tetrahedron, special algorithms can be used for solving these linear matrix system to speed up the calculation.

1.4.3 Mass-Tensor Model

In MTM, the object is discretized with tetrahedral meshes as shown in Fig. 6.

Similar to the finite element theory, the displacement inside each tetrahedron e can be expressed by a linear interpolation of the displacement of the four vertices u_j

$$\mathbf{u}(\mathbf{x}) = -\sum_{j=0}^{3} \frac{\mathbf{m}_j \cdot (\mathbf{x} - \mathbf{p}_{j+1})}{6V^e} \mathbf{u}_j \tag{24}$$

where V^e is the initial volume of tetrahedron e, and $\mathbf{m}_j$ is the area vector defined by

$$\mathbf{m}_j = (-1)^{j+1} \left(\mathbf{p}_{j+1} \times \mathbf{p}_{j+2} + \mathbf{p}_{j+2} \times \mathbf{p}_{j+3} + \mathbf{p}_{j+3} \times \mathbf{p}_{j+1} \right) \tag{25}$$

The nodal force exerted at jth vertex of tetrahedron e is defined as the derivative of the elastic energy:

Table 1 Hyperelastic material models

St-Venant Kirchoff	$w = \frac{\lambda}{2}(tr\mathbf{E})^2 + \mu tr\mathbf{E}^2$
Neo-Hookean	$w = \frac{\mu}{2}tr\mathbf{E} + f(I_3)$
Fung isotropic	$w = \frac{\mu}{2}e^{tr\mathbf{E}} + f(I_3)$
Fung anisotropic	$w = \frac{\mu}{2}e^{tr\mathbf{E}} + \frac{k_1}{k_2}\left(e^{k_2(I_4-1)} - 1\right) + f(I_3)$
Veronda–Westman	$w = c_1 e^{\gamma tr\mathbf{E}} + c_2 tr\mathbf{E}^2 + f(I_3)$
Mooney–Rivlin	$w = c_{10}tr\mathbf{E} + c_{01}tr\mathbf{E}^2 + f(I_3)$

$$\mathbf{f}_j^e = -\frac{\partial W}{\partial \mathbf{p}_j} \tag{26}$$

where elastic energy required to deform a body can be expressed as a function of the invariants ($I_1 = tr\mathbf{E}, I_2 = tr\mathbf{E}^2, I_3 = det\mathbf{E}$) of strain tensor $\mathbf{E}$:

$$W = \int w(I_1, I_2, I_3)dX \tag{27}$$

There are several hyperelastic material models are available as shown in Table 1.

By using St-Venant Kirchoff elastic enery model in Table 1 and linearized strain tensor in Eq. 9, the following equation can be deduced:

$$\mathbf{f}_j^e = \sum_{k=0}^{3} \mathbf{K}_{jk}^e \mathbf{u}_k \tag{28}$$

where the 3×3 stiffness tensors $\mathbf{K}_{jk}^e$ is expressed as

$$\mathbf{K}_{jk}^e = \frac{1}{36V^e}\left(\lambda(\mathbf{m}_j \otimes \mathbf{m}_k) + \mu(\mathbf{m}_k \otimes \mathbf{m}_j) + \mu(\mathbf{m}_j \cdot \mathbf{m}_k)\mathbf{I}\right) \tag{29}$$

Here the area vector is defined by Eq. 25, its tensor product is defined by $\mathbf{a} \otimes \mathbf{b} = \mathbf{a}\mathbf{b}^T$, and V^e is the initial volume of tetrahedron e.

The total elastic force exerted on vertex j is the sum of the local force across all tetrahedra containing vertex j:

$$\mathbf{f}_j = \sum_{\forall e \in \Omega_j} \mathbf{f}_j^e = \sum_{\forall e \in \Omega_j} \sum_{k=0}^{3} \mathbf{K}_{jk}^e \mathbf{u}_k \tag{30}$$

where Ω_j is the collection of all tetrahedra connected to vertex j.

By rewriting Eq. 30 into vertex and edge components, one can obtain the following final expressions for forces at each node j

$$\mathbf{f}_j = \mathbf{K}_{jj}\mathbf{u}_j + \sum_{\forall k \in \Psi_j} \mathbf{K}_{jk}\mathbf{u}_k \tag{31}$$

where $\mathbf{K}_{jj} = \sum_{e \in \Omega_j} \mathbf{K}_{jj}^e$, $\mathbf{K}_{jk} = \sum_{e \in \Omega_j} \mathbf{K}_{jk}^e$, and Ψ_j is the collection of all the neighboring vertices connected to vertex j.

Since the stiffness tensors are only dependent on initial mesh configuration and material properties, they can be pre-computed and applied to various boundary conditions without re-computation.

By introducing direct computation [52], the solution can be obtained in iterative manners.

$$\mathbf{u}_j^t = -\mathbf{K}_{jj}^{-1} \left(\sum_{\forall k \in \Psi_j} \mathbf{K}_{jk} \mathbf{u}_k^{t-1} \right) \tag{32}$$

2 Essential Procedures for Facial Soft-Tissue Simulation

Facial soft-tissue simulation consists of mainly five sub-tasks as shown in Fig. 7: image acquisition, tissue modeling, boundary condition, and tissue property assignment, actual simulation. The detailed description on each step will be presented in the following sub-sections.

2.1 Image Acquisition

CT scan is commonly used as a standard protocol for computer-assisted 3D planning. Since Magnetic Resonance Imaging (MRI) scan is needed to extract sub-anatomical soft structures. However, it is still required to have laborious efforts to segment anatomical structures from MRI scans. Additionally, 3D scan data can provide up-to-date outer skin profile with texture in high-precision. During image acquisition, it is highly recommended not to have any unnatural soft-tissue deformation caused by external forces (e.g. fixation bandage), and to ensure an appropriate imaging field-of-view (FOV) covering the whole frontal soft-tissue region, as shown in Fig. 8.

2.2 Tissue Modeling

2.2.1 Segmentation of Hard and Soft-Tissue

Generally, extraction of bony structures can be automatized on CT scans by using simple intensity-based thresholding. On the other hand, segmentation of soft-tissue requires certain amount of manual adjustment. Image-based segmentation tools, such as lasso or magic wand in imaging software, such as Amira (Mercury Computer Systems, Germany), can be effectively used to accelerate manual segmentation

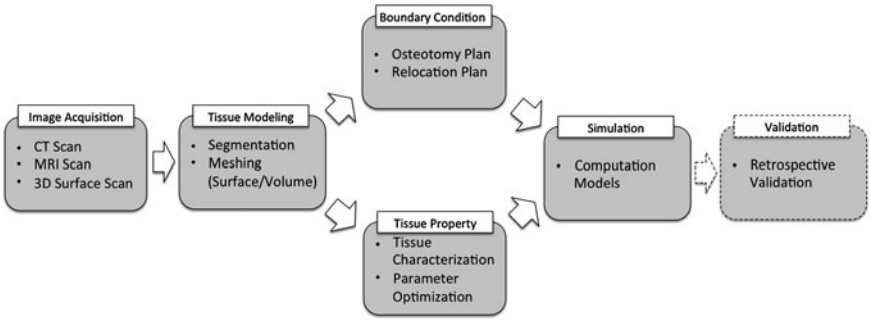

Fig. 7 General steps to solve soft-tissue simulation problem

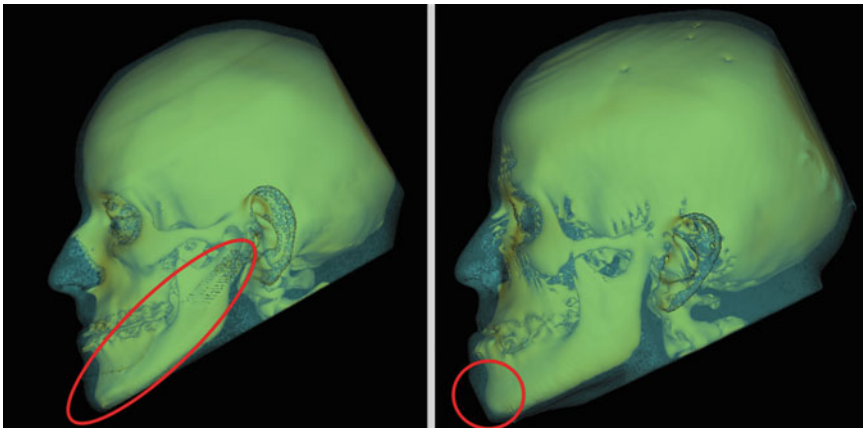

Fig. 8 Examples of undesirable scans: unnatural deformation caused by fixation bandage (*left*), FOV does not cover the whole frontal soft-tissue region (*right*)

procedures. As for advanced segmentation method, level-set based segmentation has been applied for segmentation of extra-cranial soft-tissue layer [36], and has proved to be effective in defining weak boundaries between intra- and extra-cranial soft-tissue. Additional efforts might be needed if it is required to separate upper and lower jaw around temporomandibular joint (TMJ). Furthermore, it is quite common to have streak artifacts caused by metal filling on patient's teeth, which makes segmentation task difficult for both hard and soft-tissues, as shown in Fig. 9 [34].

2.2.2 Surface and Volumetric Meshing

Based on the segmentation result, surface mesh can be generated using conventional marching cube algorithm [33], followed by automatized tetrahedral volumetric mesh generation will be followed. Due to strict limitation in converting

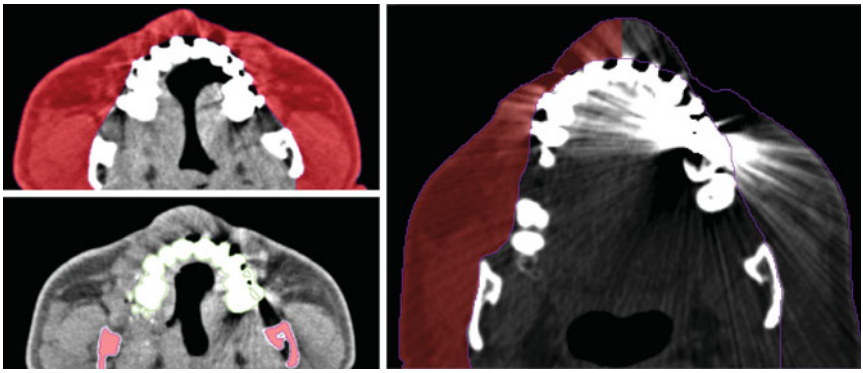

Fig. 9 Segmentation of extra-cranial soft-tissue and bony structures (*left*), metal streak artifacts are commonly present in clinical CT scans (*right*)

surface mesh to volumetric mesh, certain amount of iterative refinement in segmentation result is commonly required.

2.3 Boundary Condition Assignment

Once both entire hard- and soft-tissue models are created, bony segments can be prepared by the osteotomy planning software. Each movable part will define the corresponding contact regions with soft-tissue model. Then, a relocation planning module will define the planned movement of the parts, which will provide the corresponding movement of the affected regions on the soft-tissue.

As shown in Fig. 10, volumetric nodes are classified into four types: fixed, joined, sliding and free nodes. Fixed nodes are defined along the most posterior plane of volumetric soft-tissue model, which can be assumed to be fixed during the simulation. Joined nodes are defined on the interface between relocated bone segments and soft-tissue, which are defined by the osteotomy and relocation plan. Additionally, sliding nodes are defined on the interface around the teeth and mucosa area.

Sliding nodes has been modeled by putting additional springs between soft- and hard-tissue layers in MSM [51], and considering only tangential component of local force in bone–tissue interface using MTM [25, 26].

2.4 Tissue Property Assignment

The characterization of soft-tissue properties can be performed in the following ways, as shown in Fig. 11.

- In vitro rheology

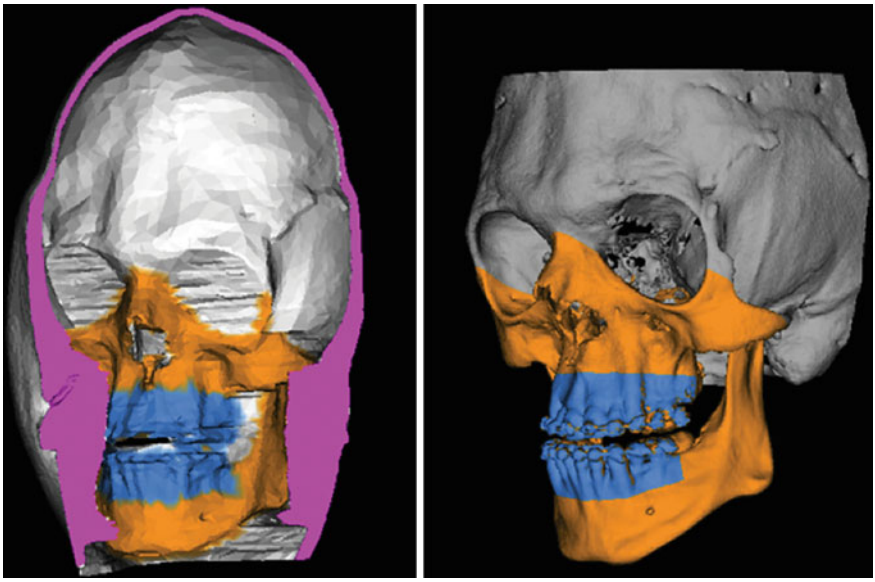

Fig. 10 Classification of volumetric nodes: fixed (*pink*), joined (*orange*), sliding (*blue*) and free (*white*)

- In vivo rhelogy
- In silico rhelogy
- Elastometry

In vitro rheology can be performed in a laboratory using loading devices with matured technique. However, it is not suitable for soft-tissue due to perfusion. In vivo rheology can provide stress–strain relationships at several locations. However, influence of boundary condition in real biological tissues is not well understood. In silico rheology is suitable for surgery simulation, which is based on computational approaches. The physical parameters can be deduced by the optimization process [38, 60]. Elastometry based on MRI or ultrasound imaging can provide non-invasive ways to measure internal tissue properties. However, it is only validated for linear elastic materials.

2.5 Simulation

The calculation of deformation has to be performed based on the computational methods presented in Sect. 1.4. The computational models could be selected depending on the limiting factors of the application, e.g. pre-processing difficulty, computation time or level of required accuracy.

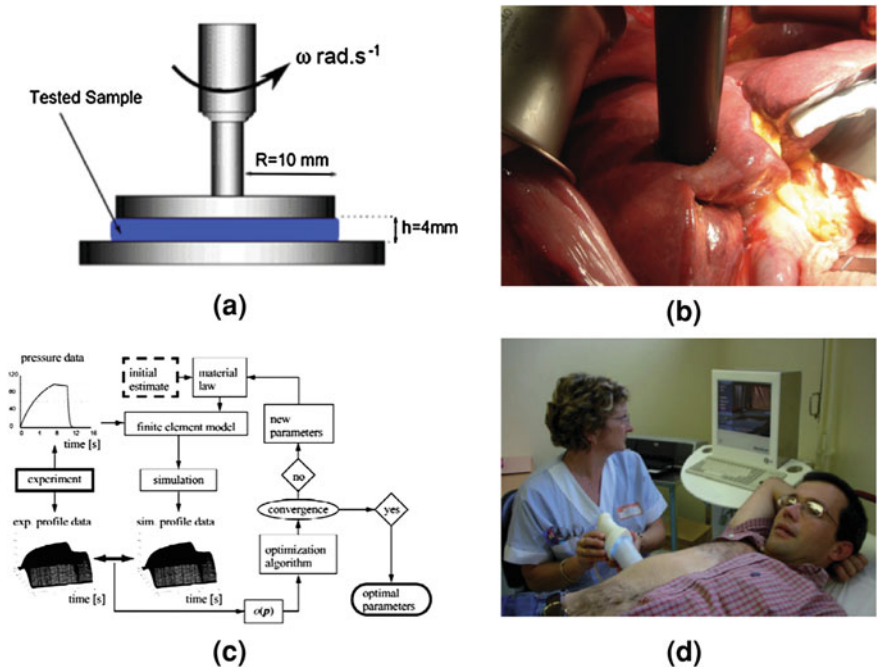

Fig. 11 Various tissue characterization methods: (**a**) In vitro rheology [35] (**b**) In-vivo rheology [41] (**c**) In silico rheology [23] (**d**) Elastometry [31]

2.6 Validation

In order to assess the simulation accuracy, normally retrospective validation scheme is used, which compares the surface to surface distance between the simulation result and actual post-operative result. Since there is no guarantee that actual operation has been performed as it is planned, the actual displacement of bone segments during the operation has to be reproduced by matching the pre-operative and post-operative images. First, the post-operative data needs to be aligned with pre-operative data by using volumetric image registration method on the unaltered skull part, such as skull-base, as shown in Fig. 12 (*left*). Then, the actual bone-related planning is reproduced by performing ICP-based surface registration between pre- and post-operative bone segments, see Fig. 12 (*right*) [2].

For simplicity, the distance between simulation and post-operative result has been measured based on closest matched points. However, this could result in underestimation of true discrepancy between simulation result and actual outcome. In order to produce a more reliable assessment, the surface-to-surface distance should be measured between anatomically corresponding points. Several methods based on Thin-Plate-Spine + Rapid Point Matching (TPS+RPM) [39], Spherical

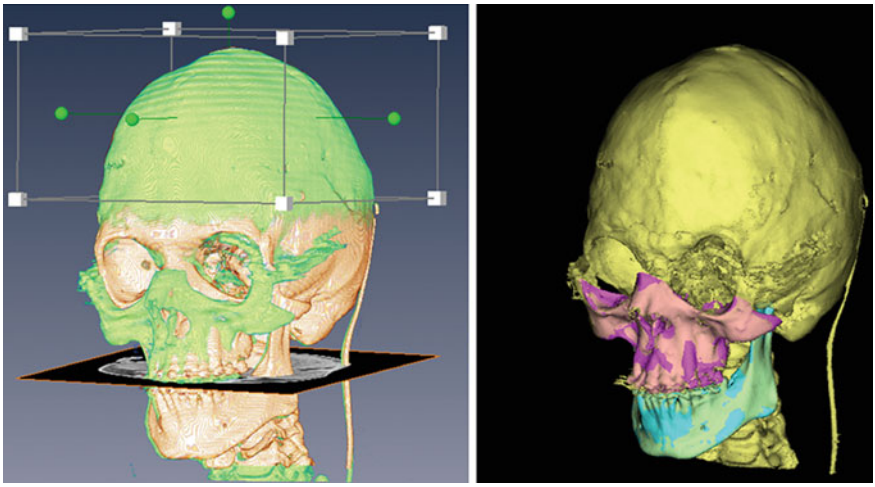

Fig. 12 Reproduction of bone-related planning for retrospective validation study: registration of pre- and post-operative images (*left*), registration of pre-operative bone segments to post-operative yellow skull model (*right*)

Harmonic Point Distribution Model (SPHARM-PDM) [44], Thin-Plate-Spine + Closest Point matching (TPS+CP) [25, 26] have been proposed so far.

In TPS+CP distance metric, one surface is transformed into the target surface based on manually defined corresponding anatomical landmarks, followed by anatomical corresponding points defined by a closest point matching on the deformed shape, see Fig. 13. Finally, surface-to-surface distance is measured on undeformed shape based on this revised anatomical corresponding points. Therefore, this metric can be useful for measuring surface to surface distance on deforming anatomical parts such as facial soft-tissues [25, 26].

3 Patient-Specific Facial Soft-Tissue Simulation

An example of patient-specific simulation pipeline is depicted in Fig. 14 [25, 26]. In addition to the general procedure depicted in Fig. 7, muscle modeling part is introduced in order to incorporate patient-specific facial muscles. The detailed description on patient-specific consideration on this study will be presented in the following sub-sections.

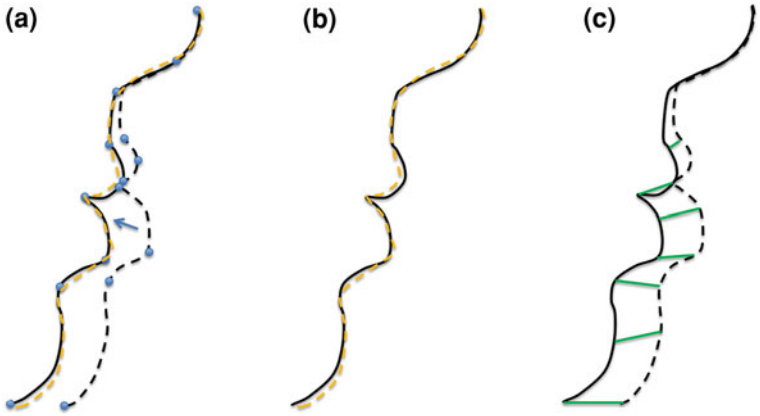

Fig. 13 TPS+CP based surface-to-surface distance measurement: (**a**) landmark-based implicit TPS transform of original geometry, (**b**) closest point matching on transformed shape, (**c**) anatomically adjusted correspondences

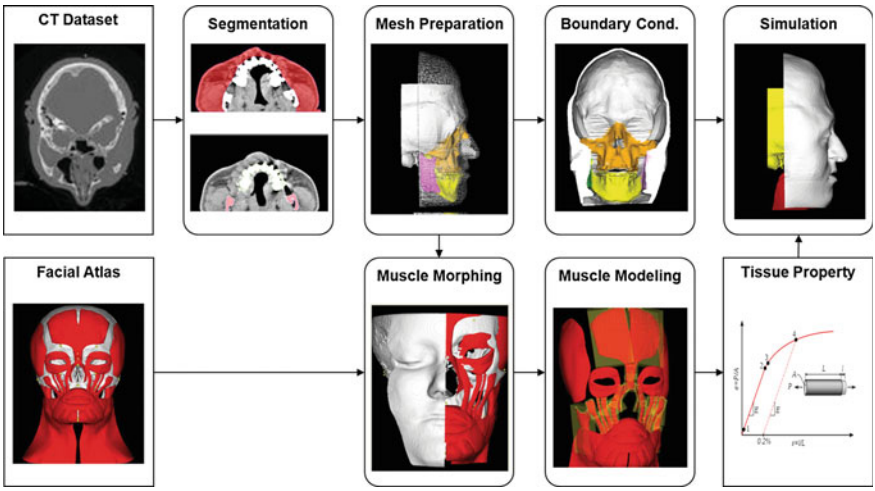

Fig. 14 The pipeline of the anatomically considered facial soft-tissue simulation method

3.1 Facial Muscle Modeling

It is almost impossible to identify individual muscles from clinical CT scan. Even with MR scan, which is not included in a typical clinical workflow, segmentation of individual muscles is still a challenging and time-consuming task. In order to

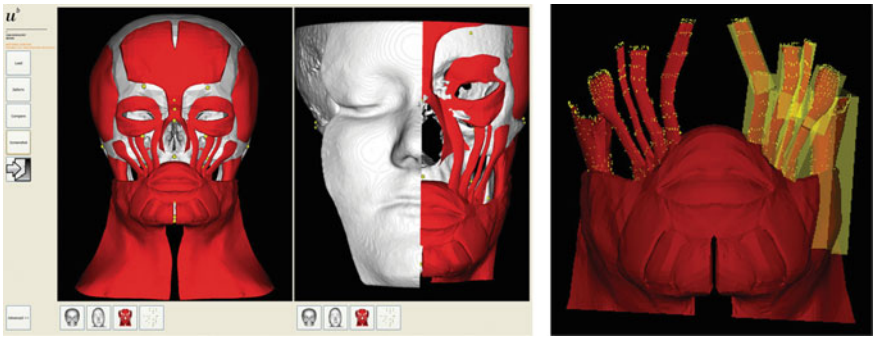

Fig. 15 Morphing of template muscles to patient-specific anatomy (*left*), and extraction of morphed muscle direction using oriented-bounding boxes (*right*)

minimize the efforts on facial muscles segmentation, construction of patient-specific facial muscles was considered through a template-to-patient deformation process. Publicly available facial template model [49] was used. The morphing procedure was driven by landmark-based thin-plate-spline (TPS) deformation [4] based on 32 anatomical landmarks, which are commonly used for measuring skin depth in forensic science [45].

In order to obtain the direction of muscles, oriented-bounding boxes (OBB) were extracted for linear-type muscles. As shown in Fig. 15, the number of OBBs for individual muscle can be adjusted according to the curvature of the muscle. For example, the masseter muscle was represented by single OBB, while the other muscles were represented by double OBBs. The longitudinal direction of each bounding box was regarded as the direction of muscle for each segment.

3.2 Equivalent Tissue Property Assignment

Up to our knowledge, there was no consensus in the literature on mechanical properties of facial soft-tissue. Different material parameters have been proposed in previous works depending on the characterization method and material model. Consequently, Young's modulus of muscle tissue along and across fiber direction were adopted from a previous study [11]. Previous works on estimating optimal facial tissue properties by comparing their simulation models with real post-operative data [38, 60] were referred to as well. The parameters that we selected for our simulation are shown in Table 2. Since there was no previous study found on anisotropic Poisson ratio of muscle, isotropic Poisson ratio was adopted.

Since it is difficult to remesh volumetric facial tissue according to the intersection with muscle surfaces, the equivalent material property was calculated by considering the volumetric proportion of muscle in each tetrahedron. The approach

Table 2 Material properties used for simulation

	Young's modulus (MPa)	Poisson ratio
Fat	0.003	0.46
Muscle across fiber	0.79	0.43
Muscle along fiber	0.5	0.43

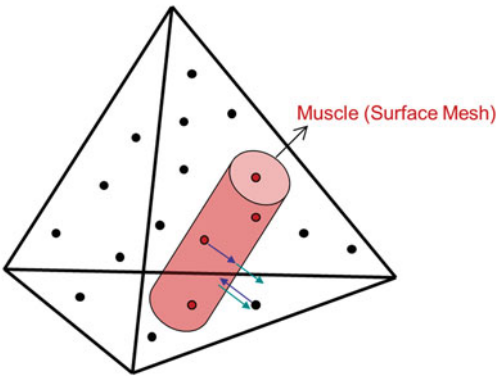

Fig. 16 Calculation of intersecting portion of muscle in each tetrahedron. Random points (*black dots*) are generated inside a tetrahedron and geometrical tests, described by the *arrows*, allow definition of material properties

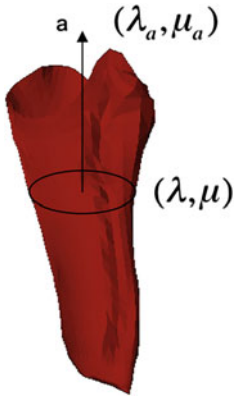

Fig. 17 Definition of Lamé coefficients along the direction of muscle

proposed by Uesu et al. [55] was adopted, which employs point sampling in tetrahedron. Then, geometrical test, based on directional comparison of surface normal and closest distance vector, as shown in Fig. 16, was performed to calculate equivalent material properties.

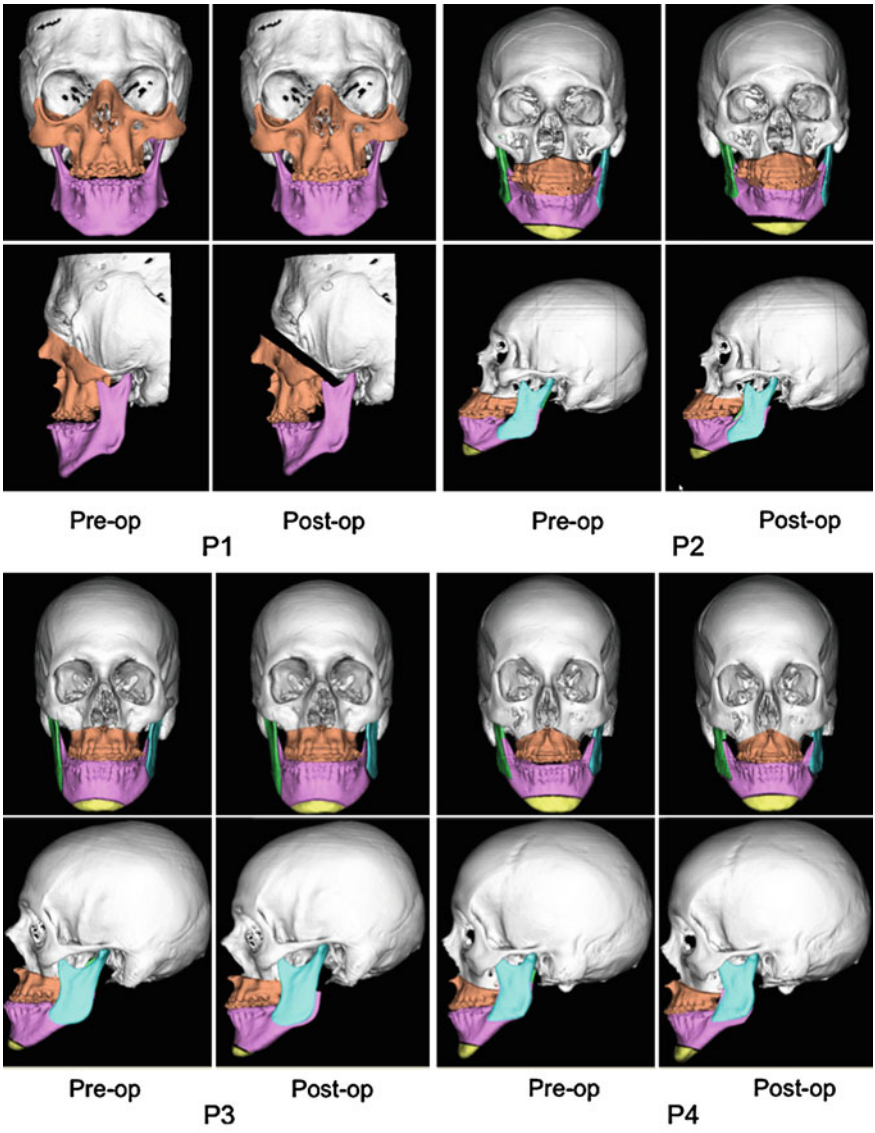

Fig. 18 Reproduced relocation planning of four clinical cases. On each case pre- and post-operative situation is displayed, with different colors representing the main structures of interest for the surgical procedures

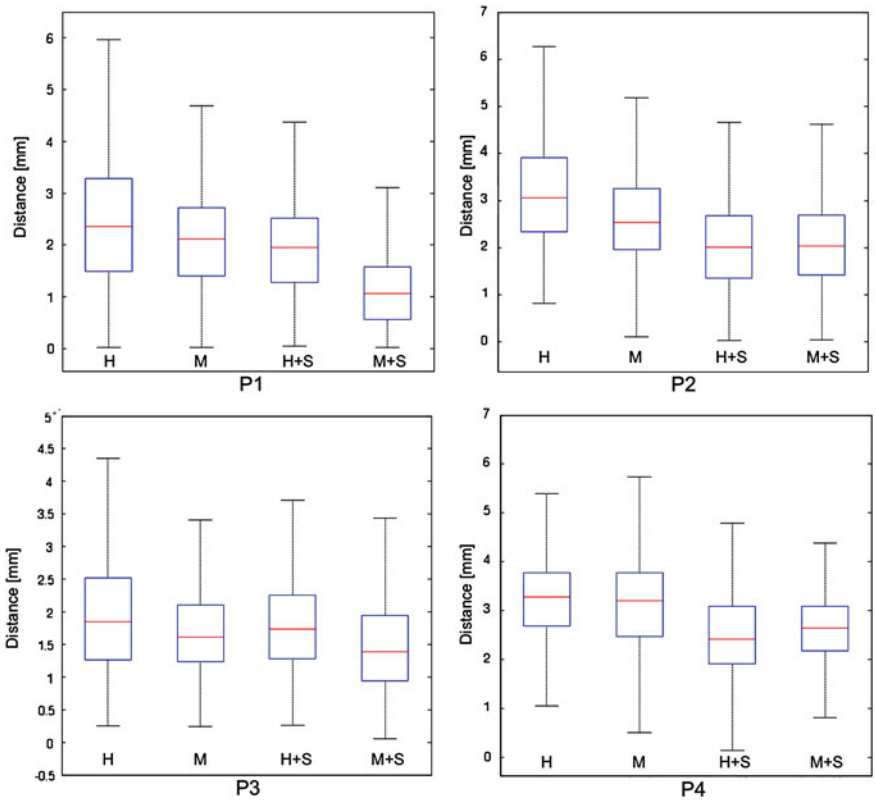

Fig. 19 Boxplot of distance errors between simulations and post-operative result for four clinical cases (P1, P2, P3, P4); Each graph represents the results with homogeneous (H), muscle template (M), homogeneous + sliding contact (H+S), and muscle template + sliding contact (M+S)

3.3 Transversely-Isotropic Mass-Tensor Modeling

The extension to transversely isotropic MTM can be achieved by adding 3×3 anisotropic stiffness tensor term to isotropic stiffness tensor in Eq. 29 [47], where the differences in Lamé coefficients along and across the muscle direction are defined by $\triangle\lambda = \lambda_a - \lambda, \triangle\mu = \mu_a - \mu$(Fig. 17).

$$\begin{aligned}\mathbf{A}^e_{jk} = \mathbf{K}^e_{jk} + \frac{1}{144V^e}(&\triangle\lambda(\mathbf{a}\cdot\mathbf{m}_k)(\mathbf{m}_j\otimes\mathbf{a})\\ &-(\triangle\lambda+2\triangle\mu)(\mathbf{a}\cdot\mathbf{m}_j)(\mathbf{a}\cdot\mathbf{m}_k)(\mathbf{a}\otimes\mathbf{a})\\ &+\triangle\mu(\mathbf{a}\cdot\mathbf{m}_k)(\mathbf{a}\otimes\mathbf{m}_j)+\triangle\mu(\mathbf{a}\cdot\mathbf{m}_j)(\mathbf{m}_k\otimes\mathbf{a})\\ &+\triangle\mu(\mathbf{m}_j\cdot\mathbf{m}_k)(\mathbf{a}\otimes\mathbf{a})+\triangle\mu(\mathbf{a}\cdot\mathbf{m}_j)(\mathbf{a}\cdot\mathbf{m}_k)\mathbf{I})\end{aligned} \tag{33}$$

Table 3 Statistical results for four patient data

		Average error	Standard deviation	90th Percentile	95th Percentile
P1	H	2.50	1.21	4.10	4.40
	M	2.21	1.23	3.39	4.16
	H+S	2.07	1.24	3.68	4.39
	M+S	1.21	0.92	2.15	2.90
P2	H	3.25	1.27	5.13	5.85
	M	2.68	1.07	4.00	4.65
	H+S	2.11	1.06	3.42	4.06
	M+S	2.14	0.98	3.42	4.04
P3	H	2.03	2.41	3.01	3.38
	M	1.80	2.36	2.61	2.87
	H+S	1.75	0.71	2.61	2.78
	M+S	1.58	1.90	2.58	2.84
P4	H	3.23	0.83	4.25	4.48
	M	3.10	0.99	4.27	4.51
	H+S	2.43	0.84	3.46	3.67
	M+S	2.56	0.74	3.39	3.62

The further extension to non-linear MTM can be achieved by introducing the complete Green–St.Venant strain tensor in Eq. 8 into St.Venant–Kirchhoff model [46].

3.4 Validation with Clinical Cases

In order to assess the accuracy of the proposed patient-specific simulation strategy, the retrospective validation of four clinical cases was performed. The actual bone-related plannings were reproduced by the procedures presented in Sect. 2.6, and are shown in Fig. 18.

The simulation of homogeneous and transversely isotropic elasticity tissue models was conducted, and accuracy in different tissue models was compared. In addition, sliding contact was also considered as part of the simulation. For the calculation of surface-to-surface distance, the TPS+CP distance measurement scheme, presented in Sect. 2.6, was used.

As shown in Fig. 19 and Table 3, there was a statistically significant decrease in mean surface-to-surface distance by incorporating transversely isotropy of muscles and sliding contact. The statistical significance was confirmed by Wilcoxon test ($p < 0.05$). The qualitative improvements can be visualized by color-mapped distance errors, as shown in Fig. 20. The negative value means that predicted skin surface lies inside the post-operative skin surface.

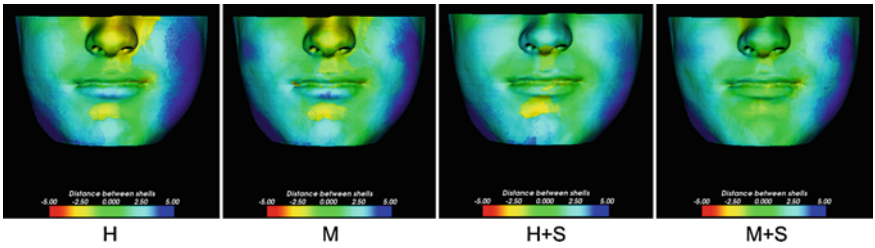

Fig. 20 Example of color-mapped distance map between simulations for patient three; Colormap starts from red to blue in the range of [−5 mm, 5 mm]

4 Conclusions

There have been various computational methods developed for simulating facial soft-tissue. Each computational model can be selected depending on its own characteristics. In order to enhance simulation accuracy, patient-specific soft-tissue simulation for CMF surgery has been developed and retrospectively validated with post-operative CT data. As for minimizing efforts for building patient-specific models, a subject-specific template-based morphing technique has been proposed. The directional behavior of facial muscles has been modeled with computationally efficient transversely-isotropic MTM. By introducing sliding boundary condition on error-sensitive regions, the simulation accuracy has been improved in statistically significant amount.

Acknowledgements This work was supported by the Swiss National Center of Competence in Research "Computer Aided and Image Guided Medical Interventions (Co-Me)", and the AO/ASIF Foundation, Davos, Switzerland.

References

1. Barich, F.: Class II, division 2 (angle) malocclusion: report of a case. Am. J. Orthod. **37**(4), 286–293 (1951)
2. Besl, P., McKay, H.: A method for registration of 3-d shapes. Pattern Anal. Mach. Intell. IEEE Trans. **14**(2), 294–299 (1992)
3. Bianchi, A., Muyldermans, L., Martino, M.D., Lancellotti, L., Amadori, S., Sarti, A., Marchetti, C.: Facial soft tissue esthetic predictions: validation in craniomaxillofacial surgery with cone beam computed tomography data. J. Oral. Maxillofac. Surg. **68**(7), 1471–1479 (2010)
4. Bookstein, F.: Principal warps: thin-plate splines and the decomposition of deformations. Pattern Anal. Mach. Intell. IEEE Trans. **11**(6), 567–585 (1989)
5. Chabanas, M., Luboz, V., Payan, Y.: Patient specific finite element model of the face soft tissues for computer-assisted maxillofacial surgery. Med. Image. Anal. **7**(2), 131–151 (2003)
6. Chapuis, J., Schramm, A., Pappas, I., Hallermann, W., Schwenzer-Zimmerer, K., Langlotz, F., Caversaccio, M.: A new system for computer-aided preoperative planning and intraoperative

navigation during corrective jaw surgery. Inf. Technol. Biomed. IEEE Trans. **11**(3), 274–287 (2007)
7. Cotin, S., Delingette, H., Ayache, N.: A hybrid elastic model for real-time cutting, deformations, and force feedback for surgery training and simulation. Vis. Comput. **16**(8), 437–452 (2000)
8. Cunningham, M.: Measuring the physical in physical attractiveness: quasi-experiments on the sociobiology of female facial beauty. J. Pers. Soc. Psychol. **50**(5), 925–935 (2000)
9. Cunningham, M., Roberts, A.: "Their ideas of beauty are, on the whole, the same as ours": consistency and variability in the cross-cultural perception of female physical attractiveness. J. Pers. Soc. Psychol. **68**(2), 261–279 (1995)
10. Downs, W.B.: Variations in facial relationships; their significance in treatment and prognosis. Am. J. Orthod. **34**(10), 812–840 (1948)
11. Duck, F.A.: Physical Properties of Tissue: A Comprehensive Reference Book, Academic Press, London (1990)
12. Dürer A.:Vier Bücher von menschlicher Proportion. Nürnberg (1528)
13. Ewers, R., Schicho, K., Undt, G., Wanschitz, F., Truppe, M., Seemann, R., Wagner, A.: Basic research and 12 years of clinical experience in computer-assisted navigation technology: a review. Int. J. Oral. Maxillofac. Surg. **34**(1), 1–8 (2005)
14. Fung, Y.C.: Biomechanics: Mechanical Properties of Living Tissues. Springer, New York (1993)
15. Gelder, A.V.: Approximate simulation of elastic membranes by triangulated spring meshes. J. Graph. Tools **3**(2), 21–42 (1998)
16. Gladilin, E.: Biomechanical modeling of soft tissue and facial expressions for craniofacial surgery planning. Ph.D. thesis, Free University Berlin (2003)
17. Hopkin, G.B.: The growth factor in the prognosis of treated cases of angle class 3 malocclusion. Rep. Congr. Eur. Orthod. Soc. **41**, 353–363 (1965)
18. Hume, D.: A treatise of human nature. http://www.books.google.com (2003)
19. Johnston, V.S., Solomon, C.J., Gibson, S.J., Pallares-Bejarano, A.: Human facial beauty: current theories and methodologies. Arch. Facial. Plast. Surg. **5**(5), 371–377 (2003)
20. Juergens, P., et al.: A computer-assisted diagnostic and treatment concept to increase accuracy and safety in the extracranial correction of cranial vault asymmetries. J. Oral. Maxillofac. Surg. (2011, in press)
21. Juergens, P., Klug, C., Krol, Z., Beinemann, J., Kim, H., Reyes, M., Guevara-Rojas, G., Zeilhofer, H.F., Ewers, R., Schicho, K.: Navigation-guided harvesting of autologous iliac crest graft for mandibular reconstruction. J. Oral. Maxillofacial. Surg. (2011, in press)
22. Juergens, P., Ratia, J., Beinemann, J., Krol, Z., Schicho, K., Kunz, C., Zeilhofer, H.F., Zimmerer, S.: Enabling an unimpeded surgical approach to the skull base in patients with cranial hyperostosis, exemplarily demonstrated for craniometaphyseal dysplasia. J. Neurosurg. **115**, 528–535 (2011)
23. Kauer, M., Vuskovic, V., Dual, J., Szekely, G., Bajka, M.: Inverse finite element characterization of soft tissues. Med. Image. Anal. **6**(3), 275–287 (2002)
24. Keeve, E., Girod, S., Kikinis, R., Girod, B.: Deformable modeling of facial tissue for craniofacial surgery simulation. Comput. Aided Surg. **3**(5), 228–238 (1998)
25. Kim, H., Juergens, P., Weber, S., Nolte, L.: A new soft-tissue simulation strategy for craniomaxillofacial surgery using facial muscle template model. Prog. Biophys. Mol. Biol. **103**(2–3), 284–291 (2010)
26. Kim, H., Jürgens, P., Nolte, L., Reyes, M.: Anatomically-driven soft-tissue simulation strategy for cranio-maxillofacial surgery using facial muscle template model. Med. Image Comput. Comput.-Assist. Interv. **6361**, 61–68 (2010)
27. Koch, R.M., Gross, M.H., Carls, F.R., von Büren, D.F., Fankhauser, G., Parish, Y.I.H.: Simulating facial surgery using finite element models. In: Proceedings of ACM SIGGRAPH, pp. 421–428. ACM Press, New York (1996)
28. Langlois, J., Roggman, L.: What is average and what is not average about attractive faces? Psychol. Sci. **5**, 214–220 (1994)

29. Langlois, J., Roggman, L., Casey, R.: Infant preferences for attractive faces: rudiments of a stereotype? Dev. Psychol. **23**(3), 363–369 (1987)
30. Langlois, J.H., Roggman, L.A.: Attractive faces are only average. Psychol. Sci. **1**, 115–121 (2008)
31. Ledinghen, V.D., Vergniol, J.: Transient elastography (fibroscan). Gastroenterol. Clin. Biol. **32**(6 Suppl 1), 58–67 (2008)
32. Lee, Y., Terzopoulos, D., Waters, K.: Realistic modeling for facial animation. Proceedings of the 22nd annual conference on computer graphics and interactive techniques, pp. 55–62 (1995)
33. Lorensen, W., Cline, H.: Marching cubes: a high resolution 3d surface construction algorithm. Proceedings of the 14th annual conference on computer graphics and interactive techniques, p. 169 (1987)
34. Man, B.D., Nuyts, J., Dupont, P., Marchal, G., Suetens, P.: Metal streak artifacts in X-ray computed tomography: a simulation study. Nucl. Sci. IEEE Trans. **46**(3), 691–696 (1999)
35. Marchesseau, S., Heimann, T., Chatelin, S., Willinger, R., Delingette, H.: Fast porous viscohyperelastic soft tissue model for surgery simulation: Application to liver surgery. Prog. Biophys. Mol. Biol. **103**(2–3), 185–196 (2010)
36. Mollemans, W.: Facial modelling for surgery systems. Ph.D. thesis, Katholieke Universiteit Leuven (2007)
37. Mollemans, W., Schutyser, F., Cleynenbreugel, J.V., Suetens, P.: Tetrahedral mass spring model for fast soft tissue deformation. Simulation and Soft Tissue Modeling **2673**, 145–154(2003)
38. Mollemans, W., Schutyser, F., Nadjmi, N., Maes, F., Suetens, P.: Parameter optimisation of a linear tetrahedral mass tensor model for a maxillofacial soft tissue simulator. Biomed. Simul. **4072**, 159–168 (2006)
39. Mollemans, W., Schutyser, F., Nadjmi, N., Maes, F., Suetens, P.: Predicting soft tissue deformations for a maxillofacial surgery planning system: from computational strategies to a complete clinical validation. Med. Image Anal. **11**(3), 282–301 (2007)
40. Mueller, A.A., Paysan, P., Schumacher, R., Zeilhofer, H.F., Berg-Boerner, B.I., Maurer, J., Vetter, T., Schkommodau, E., Juergens, P., Schwenzer-Zimmerer, K.: Missing facial parts computed by a morphable model and transferred directly to a polyamide laser-sintered prosthesis: an innovation study. Br. J. Oral Maxillofac. Surg. (2011, in press)
41. Nava, A., Mazza, E., Furrer, M., Villiger, P., Reinhart, W.H.: In vivo mechanical characterization of human liver. Med. Image Anal. **12**(2), 203–216 (2008)
42. Nkenke, E., Zachow, S., Benz, M., Maier, T., Veit, K., Kramer, M., Benz, S., Häusler, G., Neukam, F.W., Lell, M.: Fusion of computed tomography data and optical 3d images of the dentition for streak artefact correction in the simulation of orthognathic surgery. Dentomaxillofac. Radiol. **33**(4), 226–232 (2004)
43. Obwegeser, H.: [the one time forward movement of the maxilla and backward movement of the mandible for the correction of extreme prognathism]. SSO Schweiz Monatsschr Zahnheilkd **80**(5), 547–556 (1970)
44. Paniagua, B., Cevidanes, L., Zhu, H., Styner, M.: Outcome quantification using spharm-pdm toolbox in orthognathic surgery. Int. J. CARS **6**(5), 617–626 (2011)
45. Phillips, V., Smuts, N.: Facial reconstruction: utilization of computerized tomography to measure facial tissue thickness in a mixed racial population. Forensic Sci. Int. **83**(1), 51–59 (1996)
46. Picinbono, G., Delingette, H., Ayache, N.: Non-linear anisotropic elasticity for real-time surgery simulation. Graph. Model. **65**(5), 305–321 (2003)
47. Picinbono, G., Lombardo, J.C., Delingette, H., Ayache, N.: Anisotropic elasticity and force extrapolation to improve realism of surgery simulation. Robotics and Automation, 2000. Proceedings ICRA '00. IEEE International Conference on, vol. 1, pp. 596–602 (2000)
48. Sarti, A., Gori, R., Lamberti, C.: A physically based model to simulate maxillo-facial surgery from 3d ct images. Future Gener. Comput. Syst. **15**(2), 217–222 (1999)

49. Smith, D., Oliker, A., Carter, C., Kirov, M., McCarthy, J.: A virtual reality atlas of craniofacial anatomy. Plast. Reconstr. Surg. **120**(6), 1641 (2007)
50. Terzopoulos, D., Waters, K.: Physically-based facial modeling, analysis, and animation. J. Vis. Comput. Animat. **1**(2), 73–80 (1990)
51. Teschner, M., Girod, S., Girod, B.: Optimization approaches for soft-tissue prediction in craniofacial surgery simulation. Med. Image Comput. Comput.-Assist. Interv. **1679**, 1183–1190 (1999)
52. Teschner, M., Girod, S., Girod, B.: Direct computation of nonlinear soft-tissue deformation. Proc. Vision, Modeling, Visualization VM'00, pp. 383–390 (2000)
53. Thornhill, R.G.: Human facial beauty: average, symmetry and parasite resistance. Hum. Nat. **4**, 239–269 (1993)
54. Troulis, M.J., Everett, P., Seldin, E.B., Kikinis, R., Kaban, L.B.: Development of a three-dimensional treatment planning system based on computed tomographic data. Int. J. Oral. Maxillofac. Surg. **31**(4), 349–357 (2002)
55. Uesu, D., Bavoil, L., Fleishman, S., Shepherd, J., Silva, C.: Simplification of unstructured tetrahedral meshes by point sampling. Volume Graphics, 2005. Fourth International Workshop on, pp. 157–238 (2005)
56. Vannier, M.W., Gado, M.H., Marsh, J.L.: Three-dimensional display of intracranial soft-tissue structures. AJNR Am. J. Neuroradiol. **4**(3), 520–521 (1983)
57. Westermark, A., Zachow, S., Eppley, B.L.: Three-dimensional osteotomy planning in maxillofacial surgery including soft tissue prediction. J. Craniofac. Surg. **16**(1), 100–104 (2005)
58. Xia, J., Ip, H.H., Samman, N., Wong, H.T., Gateno, J., Wang, D., Yeung, R.W., Kot, C.S., Tideman, H.: Three-dimensional virtual-reality surgical planning and soft-tissue prediction for orthognathic surgery. IEEE Trans. Inf. Technol. Biomed. **5**(2), 97–107 (2001)
59. Zachow, S., Gladiline, E., Hege, H., Deuflhard, P.: Finite-element simulation of soft tissue deformation. Proc. CARS 2000, pp. 23–28 (2000)
60. Zachow, S., Hierl, T., Erdmann, B.: A quantitative evaluation of 3d soft tissue prediction in maxillofacial surgery planning. Proc. 3. Jahrestagung der Deutschen Gesellschaft fur Computer-und Roboter-assistierte Chirurgie eV, Munchen (2004)
61. Zeilhofer, H.F., Kliegis, U., Sader, R., Horch, H.H.: Video matching as intraoperative navigation aid in operations to improve the facial profile. Mund Kiefer Gesichtschir **1**(Suppl 1), S68–70 (1997)